Final Report for AFOSR Contract FA9550-09-C-0197

"Gravity Wave Dynamics and Tidal Interactions in the MLT and at the Bottomside F Layer and their Potential Contributions to Neutral and Plasma Dynamics"

PI: D. C. Fritts

Date: 16 April 2012

Period of Performance: 15 September 2009 to 14 June 2012

Final Report for AFOSR Contract FA9550-09-C-0197

"Gravity Wave Dynamics and Tidal Interactions in the MLT and at the Bottomside F Layer and their Potential Contributions to Neutral and Plasma Dynamics"

PI: D. C. Fritts

Date: 16 April 2012

Period of Performance: 15 September 2009 to 14 June 2012

1. Science Investigation Summary

This contract was awarded to provide observational and theoretical support of measurements aboard the C/NOFS satellite aimed at understanding equatorial neutral and plasma dynamics contributing to equatorial plasma bubble (EPB) seeding and morphology. Our specific measurement role was intended to provide ground-based observations in Brazil and Peru, including FPI measurements of F-layer winds, airglow measurements of plasma bubble drifts, and radar and digisonde measurements of electron density profiles and EPB morphology. Ancillary modeling and theoretical efforts were envisioned to include evaluation of gravity wave (GW) and tidal influences on EPB seeding conditions and statistics employing our observational data. Specific proposed research goals include:

1. *define the spatio-temporal structure and variability of equatorial F-layer neutral winds,*
2. *determine the altitude, longitude, and UT variations of the superposed tidal modes,*
3. *define the EPB structures and their altitude, longitude, and UT variations over Brazil,*
4. *assess the correlations of tidal winds with EPB occurrence and depth, especially the influences of non-migrating tidal modes (DE3) on EPB longitudinal variability, and*
5. *examine correlations of EPB occurrence with GW convective "hot-spots", and of tidal winds with GW scales and amplitudes to evaluate tidal influences on EPB seeding.*

Our approach to these research goals required redefinition due to significant reductions in the proposed funding. We have nevertheless managed to field all the ground-based instruments originally envisioned; we have also extended our measurement period by two years (to December 2011) to collect as much correlative data with the C/NOFS satellite as possible during the period of research performance. Our instrumentation employed for these studies included:

1. Fabry-Perot interferometer (FPI) F-layer wind measurements at two equatorial locations in Brazil and another three in Peru,
2. airglow instrumentation at three sites comprising a longitudinal chain in Brazil,
3. C/NOFS CERTO beacon receivers at three sites partially collocated with the airglow imagers and FPIs in eastern Brazil, and
4. VHF radar and digisonde measurements, via INPE colleagues, at Sao Luis and Fortaleza.

Additional measurements anticipated using TIMED and DMSP satellites were descoped from the research effort for lack of funding. However, we supplemented our research efforts with modeling and data analysis studies addressing GW and tidal dynamics impacting the F layer. A map of our Spread F Experiment 2 (SpreadFEx-2) instrument locations is shown in Figure 1 and our tomographic measurement strategy with the CERTO receivers and the airglow imagers, within the bi-static FPI field-of-view (FOV), are shown schematically in Figure 2.

2. Research Performed Under this Support

2.1. *SpreadFEx-2 Ground-based measurements*

Measurements supporting C/NOFS with SpreadFEx2 instrumentation began in September 2009, but without the full suite of instruments shown in Figure 1, due to funding delays and shipping schedules. As seems inevitable, remote field measurements were also impacted by equipment breakage, customs clearance, and weather. The FPIs, in particular, experienced hardware problems and customs issues, while the three CERTO receivers were not installed in Brazil until some months after our initial measurements. However, most of this equipment was in place after mid 2010, though coordination and instrument issues continued throughout our remaining measurements. In particular, the FPI and CERTO beacon receivers deployed for these measurements were operational for sufficient intervals to assemble a very valuable dataset, and enable the tomographic studies illustrated in Figure 2. The FOV overlaps between these three sites is shown in Figure 3.

An example of the initial tomography using 2 and 3 imagers is shown in Figure 4. This clearly offers an additional quantitative capability for comparing drifts with winds as a function of altitude, with horizontal and vertical resolution of ~50 and 20 km, respectively.

F-layer temperatures and winds measured by the FPI at Cajazeiros (J. Makela and J. Meriwether, Co-PIs) from initial installation through December 2011 are shown in Figure 5 and suggest the presence systematic tidal motions having both long- and shorter-term phase variations. These SpreadFEx-2 measurements have helped quantify tidal and GW winds far more precisely than was possible without FPI measurements during our earlier experiment. Bi-static FPI measurements performed during 2010 and 2011 have also enhanced our ability to quantify neutral wind influences on EPB formation and motions. Note, in particular, the tendency for increasing zonal winds in the early evening hours.

Given the progress in our wind and plasma measurements from September 2009 to March 2011, we held a meeting at INPE in Brazil to coordinate further measurements and advance our correlative analyses of these data. This proved to be highly beneficial, both in identifying potential joint research topics and in ensuring the most complete measurement plans for the final sequence of measurements.
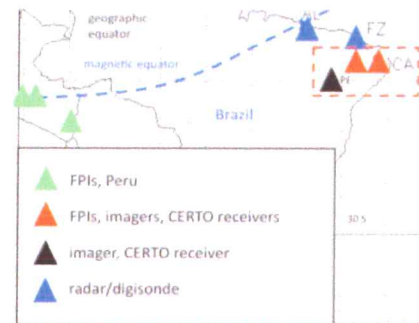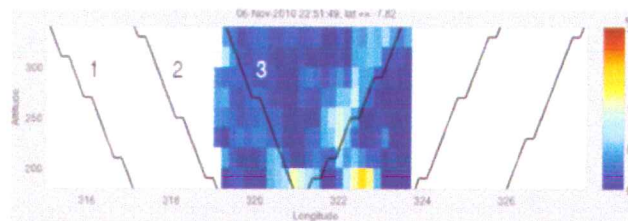

Figure 1. SpreadFEx-2 instrument locations enabled by this AFOSR contract and related efforts.
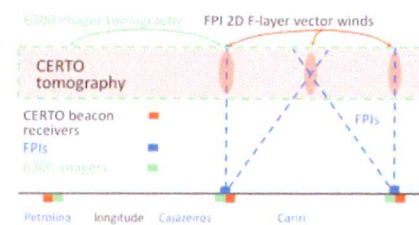
Figure 2. Tomographic and common-volume measurements envisioned for SpreadFEx-2.
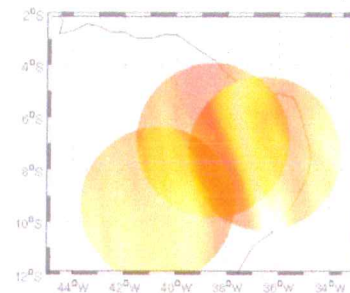
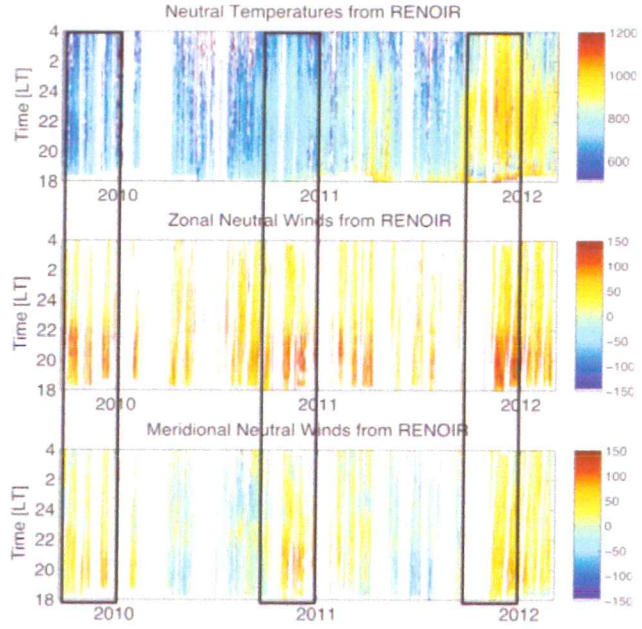**Figure 3.** Overlapping imager FOVs in the 6300 Å emission showing EPBs.

Figure 4. Preliminary EPB tomographic reconstruction using data from the 3 imagers in eastern Brazil on 6 Nov. 2009. Image spans ~319-324° longitude at ~7.8°S, black lines show FOVs of the three imagers, image outside the central 2 lines are from only 2 imagers.

Daily FPI winds proved very valuable in assessing both tidal variability and GW fluctuations at higher frequencies. Four examples from our FPI observations during November 2010 are shown for illustration in Figure 6. These readily demonstrate the value of such common-volume FPI measurements for quantifying the various waves contributing to the motion field. In particular, these winds and EPB drifts reveal both the systematic tendencies for increasing eastward winds in the early evening hours, a clear mean tidal signature evident in both Figures 5 and 6, and the potential for significant variability in these fields on a daily basis, given the clear differences between the individual panels in Figure 6. Also seen are tendencies for EPB drift velocities to lag tidal winds initially, to achieve comparable speeds as the tidal winds maximize, and to become very small in the early morning, despite sometimes significant eastward winds.

2.2. Satellite Data Analyses

A major limitation in our first SpreadFEx campaign in 2005 was a lack of sensitivity to tidal motions at the bottomside F layer and above. This was the major motivation for multiple FPIs for such measurements during SpreadFEx2. We had also hoped to employ TIMED TIDI measurements to characterize these tidal structures in redline emissions, but that proved to be outside the scope of the research selected for funding. We nevertheless were able to develop a multi-year climatology of annual and yaw-cycle mean tidal modes expected at these altitudes from CHAMP *in situ* cross-track (largely zonal) wind measurements derived from satellite drag data. These data have been employed extensively for analyses of the non-migrating tidal modes by others,

Figure 5. FPI temperatures (top), and zonal and meridional winds (middle & bottom) obtained at Cajazeiros, Brazil spanning the SpreadFEx-2 campaigns from Oct. to Dec. of 2009 to 2011.
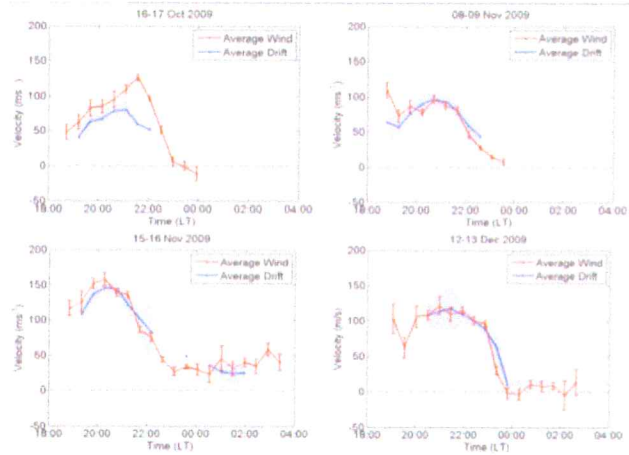
Figure 6. SpreadFEx-2 common-volume zonal winds (red) and EPB zonal drift velocity (blue) for 16-17 Oct., 8-9 Nov., 15-16 Nov., and 12-13 Dec. 2009. Note the variations at ~30-min to 2-hr periods indicative of GWs superposed on the tidal motions.

especially the diurnal eastward-propagating zonal wavenumber 3 (DE3). Hence the structures of this and other non-migrating modes are reasonably well characterized at ~400 km CHAMP altitudes. These modes typically achieve zonal amplitudes of ~5 to 15 ms^{-1} at these altitudes and exhibit annual climatologies that vary from mode to mode, with DE3 exhibiting a maximum of ~10 to 15 ms^{-1} during August.
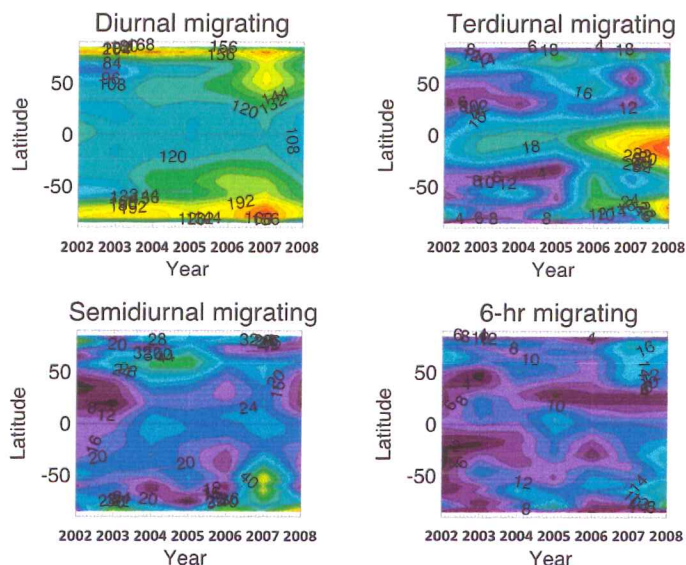
4

CHAMP data can also be used to estimate the migrating tidal modes, but surprisingly these studies were not performed previously, despite expectations that they may be substantially larger than the non-migrating modes at these altitudes, based on TIME GCM simulations performed in support of SpreadFEx. To do so in a systematic manner for the migrating modes requires averaging over a full local time precession period (~130 days), which has the potential to smooth (and reduce) amplitude estimates. We have nevertheless performed several assessments along these lines at different temporal resolutions and have indeed found very significant migrating tide amplitudes extending over ~9 years and spanning the SpreadFEx-2 measurement period. The various migrating components obtained as annual averages from 2002 to 2008 (for which CHAMP was at higher altitudes ~400 km) are shown in Figure 7. As anticipated by the TIME GCM, the total field was found to be dominated (at least averaged over a 24-hr local time precession) by the migrating diurnal tide (DW1), which achieves maxima of ~100 ms^{-1}, as predicted. The migrating semidiurnal and terdiurnal modes (SW2 and TW3) are also larger than or comparable to the corresponding non-migrating modes, suggesting that the migrating modes must contribute at least as significantly to thermospheric and ionospheric dynamics as the non-migrating modes that have received the most attention to date.

Figure 7. Annual mean diurnal, semidiurnal, terdiurnal, and 6-hr migrating tides in zonal winds from 2002 through 2008, during which CHAMP remained at ~400 km altitudes. Our analysis employed the DELFT wind data set for these assessments.

The advantages of shorter averaging times in defining thermospheric tidal variability can be seen by comparing annual mean tidal amplitudes in Figure 7 with those determined over a CHAMP yaw cycle centered on each month (thus over-sampled by ~4 times). Diurnal and semidiurnal amplitudes and phases are shown for 130-day yaw-cycle means at monthly intervals from early 2002 to late 2007 in Figure 8. Noting that the retrievals in Figure 8 show latitudes only to ±60°, the yaw-cycle means yield dramatically greater variability, as well as some sensitivity to seasonal variations in amplitude and phase. Whereas the top left panel of Figure 7 suggests a broad diurnal tide amplitude maximum centered at ~50°S extending from ~2004 to 2007, Figure 8 suggests that these are instead seasonal maxima at high southern latitudes having distinct seasonal maxima each year, with an anti-phase relation between hemispheres. Very similar features are also seen in the migrating semidiurnal tide, with southern hemisphere maxima typically from ~June to September, again with an apparent anti-correlation between hemispheres.

Also seen in Figures 7 and 8 are overall tendencies for somewhat larger amplitudes in later than in earlier years throughout the interval displayed. There are two trends that might imply amplitude variations over this interval:

1) solar cycle variations, and
2) the decay of the CHAMP altitude with time.

Of these, declining solar forcing of mean thermospheric temperatures and densities would imply increasing tidal amplitudes with time, as observed. The decline of the CHAMP altitude, however, would seem to imply decreasing amplitudes at decreasing altitudes, based on TIME GCM and other modeling of tidal propagation into the thermosphere. Hence, we consider declining solar activity during this interval to be the most likely explanation.
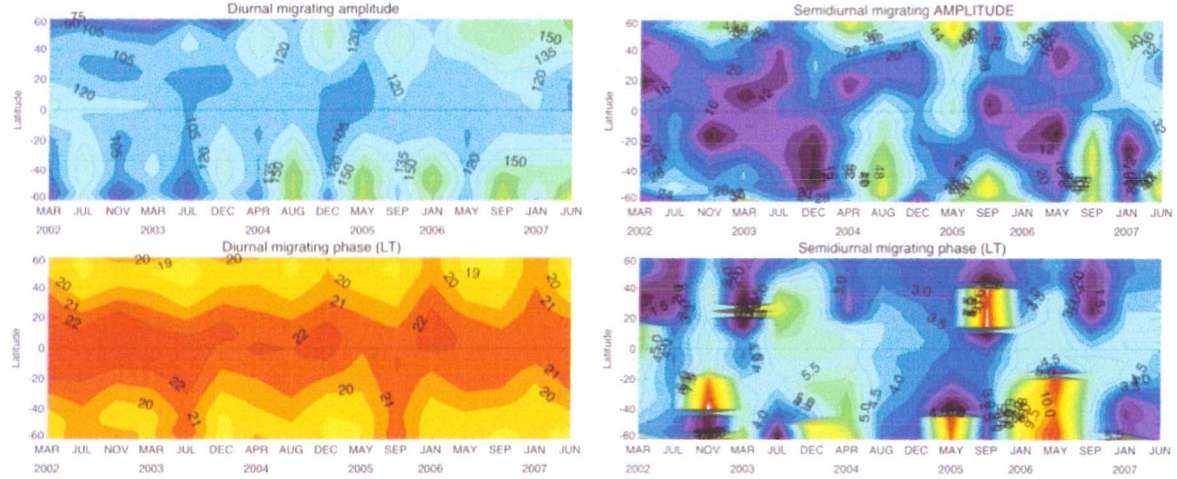

Figure 8. Yaw-cycle mean (~130 day) migrating diurnal tide zonal wind amplitudes and hour of maximum (in LT) from 2002 to 2007 (top and bottom at left) and for the migrating semidiurnal tide (at right). Note that strong phase variations seen in the lower panel often occur for small amplitudes for which phases likely exhibit large uncertainties.

CHAMP data were also employed for an initial assessment of seasonal variations of the distributions of GW variances using density fluctuations derived from CHAMP accelerometer data. This effort focused only on data obtained during CHAMP descent from its initial altitude and are thus at altitudes decreasing from ~330 km to ~250 km throughout 2010. These results reveal apparently systematic seasonal variations and consistency between ascending and descending nodes of the spacecraft. Most of the data are not relevant to EBP processes, but the earliest month (March 2010) near the end of the EPB season is shown in Figure 9 to illustrate the potential, and the apparent influences of GW sources and filtering by tidal motions at higher altitudes. These data seem to indicate a preference for responses from lower altitudes at low latitudes. We cannot speculate on the dominant effect, however, without further analysis.

2.3. Numerical Modeling of Deep Gravity Waves

We devoted significant resources during this research effort to modeling and analysis activities that we felt would provide useful guidance in the interpretation of our measurements as these became available. These focused on modeling GW dynamics
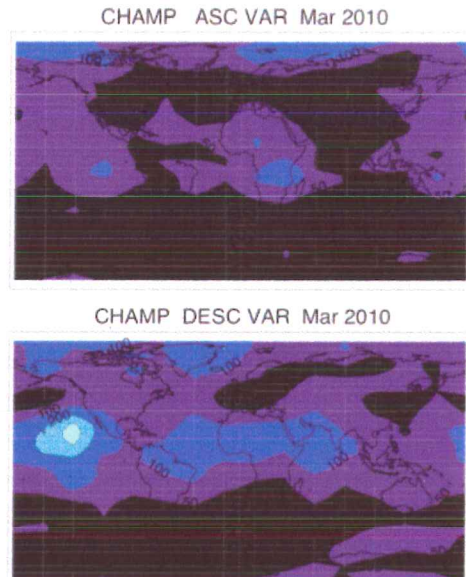

Figure 9. GW density variances computed from CHAMP data during March 2010. Note the strong equatorial and high northern latitude responses. These maps span all longitudes and latitudes to ±87°.

6

anticipated to define their possible influences at the bottomside F layer and above. Initial efforts addressed GW instabilities and interactions that are able to limit or prevent vertical propagation to high altitudes. Additional studies also began to examine responses to specific GW sources, including convection, topography, and auroral heating.

Our modeling efforts addressing instability dynamics employed 2D and 3D simulations of GWs having wavelengths spanning multiple scale heights and expected to readily penetrate well into the thermosphere and ionosphere. GWs having smaller spatial scales and phase speeds are expected to penetrate to altitudes as high as ~150 to 200 km, but not much higher due to increasing dissipation and filtering by tidal winds of ~100 ms^{-1}. As GW scales and phase speeds increase, however, their penetration altitudes increase significantly. An example of a 3D direct numerical simulation (DNS) of a relatively small-scale GW having a horizontal wavelength of λ_x = 60 km, an initial vertical wavelength of λ_z ~20 km, an initial intrinsic frequency of $\omega \sim N/10^{1/2}$, a horizontal phase speed of 55 ms^{-1}, and a horizontal perturbation velocity of u' ~5.5 ms^{-1} at 100 km is illustrated with 2D cross sections of vorticity magnitude at eight times in Figure 10. The mean temperature in this case increased from ~280 to ~900 K from 100 to 200 km and is representative of mean solar conditions. These results suggest that intermediate GW scales having sufficiently large amplitudes that arise from deep tropical convection should, on occasion at least, penetrate well into the lower thermosphere and should be expected to achieve unstable amplitudes and deep instability structures extending above ~150 km. Similar DNS for GWs having significantly larger spatial scales indicate that such motions can also penetrate to significantly higher altitudes.
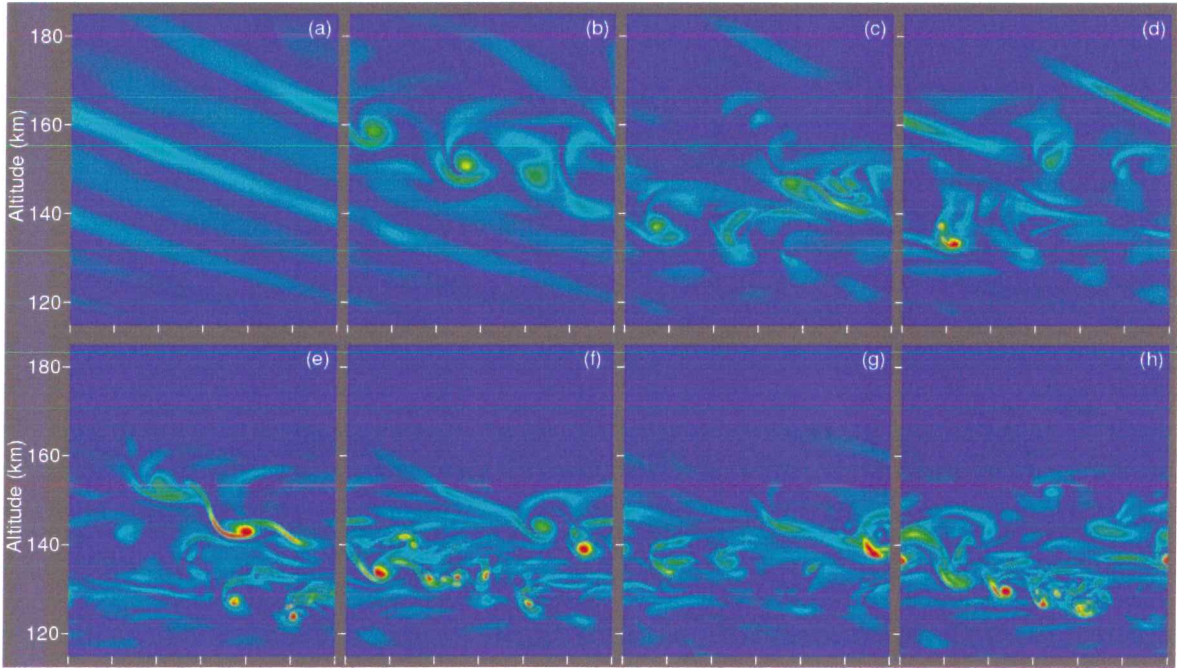

Figure 10. Streamwise-vertical cross sections of vorticity magnitude from an anelastic 3D simulation of GW breaking between ~110 and 185 km altitude spanning a time of ~90 min (after Fritts and Lund, 2010). Overturning and turbulence generation extend to altitudes of ~160 km, approximately 3 scale heights above the altitude regarded as the "turbopause". GW parameters are described in the text. GW breaking and turbulence arise due to a sufficiently large amplitude, and turbulence scales range from ~1 km at the lowest altitudes to ~5 to 10 km at the highest altitudes to which instabilities extend.

A major motivation for our anelastic DNS GW studies is our expectation that increasing GW amplitudes and scales accompanying their propagation to higher altitudes will enable quasi-linear and nonlinear dynamics that will cause their propagation and influences to depart from those anticipated by linear ray tracing methods. We expect such effects to include both those accompanying the attainment of large amplitudes by the GW and the influences of mean-flow interactions as the momentum accompanying vertical GW propagation implies strongly increasing mean-flow modifications with increasing altitude. The instability dynamics seen to occur in the DNS displayed in Figure 10 (for which the mean flow is artificially held constant) shows that instability can extend well into the thermosphere for sufficiently large GW amplitudes and spatial scales. As at lower altitudes, these instabilities also impose a limit on the GW amplitudes that can arise, and thus on their momentum transport and possible plasma perturbations that will need to be accounted for in simple descriptions of these dynamics. The GW amplitude profiles before and after wave breaking for this case are shown in Figure 11 (left).

A second influence of GWs penetrating to high altitudes is the acceleration of the mean flow accompanying increasing momentum flux (per unit density, see Figure 11, right). This acts both to alter the mean flow experienced by the trailing portion of the GW and also to accelerate the GW phase speed of the portion of the GW packet occupying the region experiencing acceleration. The former effect is well known at lower altitudes, essentially GW propagation and refraction in shear flows; the latter accompanies GWs achieving large amplitudes and mean flow accelerations comparable to the GW horizontal phase speed. This effect, known as "self acceleration", has profound implications for the GW packet structure and instability itself.

Self acceleration causes an acceleration of the GW phase speed that increases as $1/\rho(z) \sim e^{z/H}$, and becomes very significant for large-amplitudes GWs attaining high altitudes. This process both strongly distorts the GW phase structure and halts its vertical propagation, with the phase distortion contributing another instability mechanism that acts to limit the GW amplitude. The evolving phase structure of a GW undergoing self acceleration and instability is shown in Figure 12. Profiles of GW amplitude, momentum flux, and evolving $U(z)$ are shown in Figure 13. These profiles reveal that the GW packet seen in Figure 12 stalls as it achieves a large amplitude and a large induced mean wind. This is because of the implications of the kinking phase structure for vertical group velocity. Amplitude and momentum flux decreases accompany "self acceleration" instability thereafter.
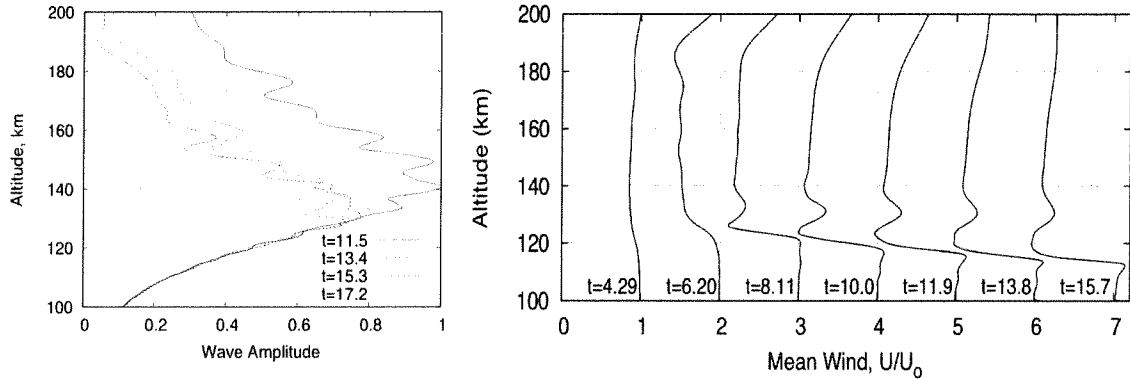
Figure 11. GW amplitude profiles (left) at t = 11.5 buoyancy periods priors to breaking, and at three later times after breaking, for a simulation in which mean flow changes were suppressed. Note the relatively constant amplitude profile with time after breaking, with decreasing amplitude with altitude reflecting viscous damping. Mean profiles (right) show large increases in mean winds approaching or exceeding the initial GW phase speed at later times when mean flow accelerations are allowed. The strong shears induced at lower altitudes are responsible for confinement of instability to these lower altitudes at later times.
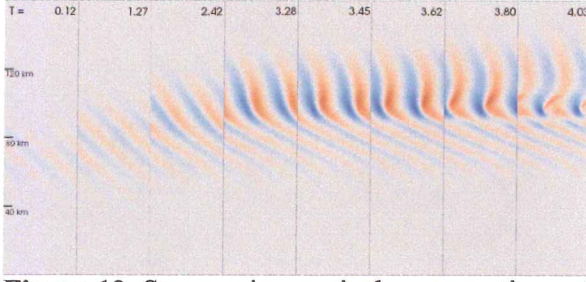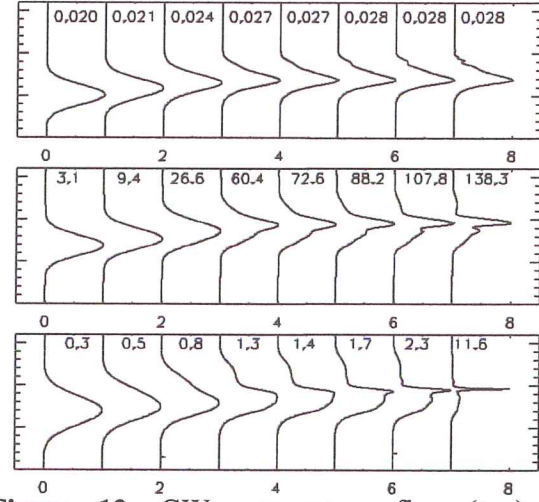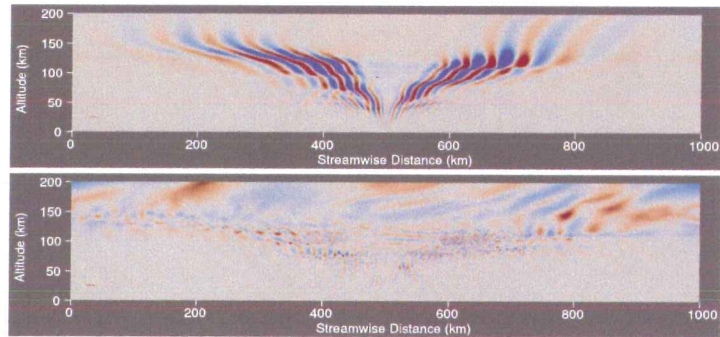
Figure 12. Streamwise-vertical cross sections of vertical velocity spanning ~4 buoyancy periods (~3 GW periods). The GW is propagating upward and to the left. Maximum vertical velocities at these times are w' are ~12, 21, 39, 67, 71, 75, 78, and 78 ms^{-1}, respectively. The kinking and increasingly complex phase structure in the right three images are indications of flow instability.

We also performed a series of simulations exploring responses to specific localized GW sources expected to yield GWs penetrating to high altitudes. One addressed the response to a single convective plume excited via a heat source extending over ~10 km in the troposphere. The environment in this case was specified by a tidal field arising from a TIME GCM simulation at 30°S (assuming convection over Brazil). We expect such simulations to be

Figure 13. GW momentum flux (top), induced mean velocity in the direction of GW propagation (middle), and amplitude (bottom) at the times shown in Figure 12. Values at the top of each profile show the peak amplitude of the respective quantity at that time. Note that the packet amplitude (estimated as u'/|c-U|) increases with altitude, the momentum flux decreases as the packet dissipates, and the induced mean flow increases strongly as mean density decreases to conserve total momentum.

far more realistic than those without varying winds, as the tides are largely responsible for the MLT wind field encountered by GWs at any latitude, though the modes and wind structures vary significantly with latitude. The resulting GW structures are shown in the perturbation potential

temperature field at ~45 and 90 min in Figure 14. Noteworthy responses include the following:

1) initial emergence of those GWs having the steepest phase fronts and highest vertical group velocities,
2) clear (and opposite) refraction of the GWs propagating in opposite directions in the tidal winds,
3) removal by critical-level instabilities of GWs having smaller phase speeds, and

Figure 14. 2D views of potential temperature field due to GWs excited by a single convective cell extending to ~10 km at ~45 and 90 min after excitation. Importantly, smaller GW scales are removed by critical-level filtering and instability and larger scales surviving to the highest altitudes have preferential propagation and momentum flux because of the tidal winds to the left at the highest altitudes.

9

4) emergence of larger-scale GWs at the higher altitudes having preferential propagation against the tidal winds at these altitudes, as predicted previously.

A second GW source we expect to have significant influences at equatorial latitudes based on a number of ground-based observations is auroral forcing. GWs inferred to have arisen from auroral sources typically have large spatial scales, high phase speeds, and periods of ~30 min to several hours. To simulate this source, we imposed a heat source having Gaussian standard deviations in latitude and altitude of 150 and 30 km, respectively, centered at 100 km, and moving southward at a speed of 200 ms^{-1}.

The response to this forcing is shown in Figure 15 at 40 minutes after GW excitation. The scales of this response are likely smaller than often accompany auroral forcing, given ground-based and satellite evidence for such GWs, but these results readily demonstrate a potential for even smaller-scale responses to penetrate to very high altitudes. Realistic atmospheric temperature and density fields were assumed, with the temperature gradient decreasing sharply above ~100 km. This accounts for the GW phase surfaces becoming steeper at the higher altitudes, as this is a consequence of a decreasing buoyancy frequency with altitude. The dominant southward-propagating portion of the response is significantly stronger because it maintains coherence with the southward motion of the source, and the GW amplitude appears to peak between ~300 and 400 km due to strongly increasing viscosity with altitude, with a Reynolds number, which describes the viscous effects on GW propagation, defined as $Re = \lambda_z^2/T_b\nu$, with λ_z, T_b, and ν the GW vertical wavelength, the buoyancy frequency, and the kinematic viscosity, respectively. In the ~300 to 400 km altitude range, Re drops rapidly below ~100, at which values the GW succumbs quickly to viscous dissipation. The anelastic FV code also has a viscous "GW radiation" upper boundary condition which allows GWs to propagate out of the domain. Hence, the decreasing GW amplitude with altitude near the upper boundary is a consequence of viscosity, not the upper boundary condition itself.
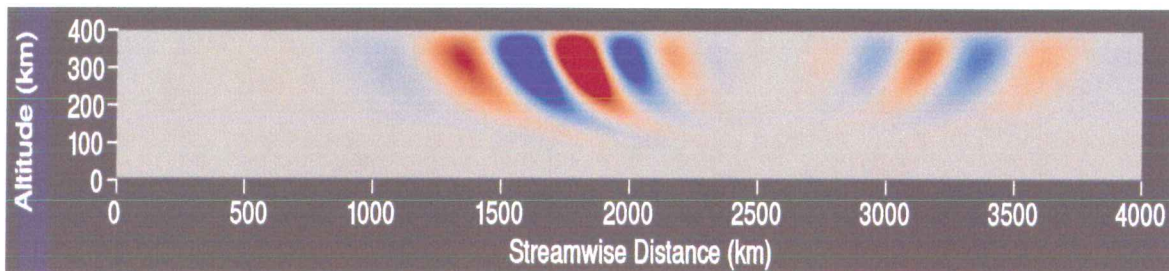
Figure 15. Vertical velocity field in a latitudinal plane arising from an idealized 2D auroral source (assumed uniform in longitude) represented as a region of Gaussian heating in latitude and the vertical (see text for details).

3. Presentations and Publications Arising from this Research (published, submitted, or in preparation)

This research spawned a large number of presentations by multiple team members at various symposia, including: AGU in 2009, 2010, and 2011; IAGA in 2009; and ISEA in 2012. Additional talks were presented are multiple workshops, including: BIRS GWs in 2010, CEDAR in 2009, 2010, and 2011; ISSI in 2010; PASI Int'l. School in 2010; IGW Workshop in 2011; and our own SpreadFEx-2 Workshop (Brazil) in 2011.

Six publications that have appeared, are submitted, or are in preparation that have arisen in part from this research to date are listed below. Others are also likely as these data are further analyzed.

Chapagain, N. P., J. J. Makela, J. W. Meriwether, D. J. Fisher, R. A. Buriti, A. F. Medeiros, Comparison of Nighttime Zonal Neutral Winds and Equatorial Plasma Bubble Drift Velocity over Brazil, J. Geophys. Res., submitted.

Fritts, D. C., R. Lieberman, and K. Hausler, 2012: GW density variances at ~250-300 km determined from CHAMP and possible implications for tidal filtering, in preparation.

Fritts, D. C., and T. Lund, 2011: Gravity wave influences in the thermosphere and ionosphere: Observations and modeling contributions, in Aeronomy of the Earth's Atmosphere and Ionosphere, Springer Academic Press, M. Abdu and D. Pancheva, Eds., Springer, 109-130.

Fritts, D. C., T. Lund, and J. Snively, 2012: Gravity wave self-acceleration effects in two and three dimensions, J. Geophys. Res., in preparation.

Lieberman, R., D. Fritts, and K. Hausler, 2012a: Migrating tides in the thermosphere at 400 km inferred from CHAMP data, Geophys. Res. Lett., in preparation.

Lund, T., and D. C. Fritts, 2012: Numerical simulation of gravity wave breaking in the lower thermosphere, J. Geophys. Res., in press.

REPORT DOCUMENTATION PAGE

Public reporting burden for this collection of information is estimated to average 1 hour per response, including the time for reviewing instructions, searching existing data sources, gathering and maintaining the data needed, and completing and reviewing this collection of information. Send comments regarding this burden estimate or any other aspect of this collection of information, including suggestions for reducing this burden to Department of Defense, Washington Headquarters Services, Directorate for Information Operations and Reports (0704-0188), 1215 Jefferson Davis Highway, Suite 1204, Arlington, VA 22202-4302. Respondents should be aware that notwithstanding any other provision of law, no person shall be subject to any penalty for failing to comply with a collection of information if it does not display a currently valid OMB control number. **PLEASE DO NOT RETURN YOUR FORM TO THE ABOVE ADDRESS.**

1. REPORT DATE *(DD-MM-YYYY)* 19-04-2012	2. REPORT TYPE Final Report	3. DATES COVERED *(From - To)* September 15, 2009 – June 14, 2012

4. TITLE AND SUBTITLE "Gravity Wave Dynamics and Tidal Interactions in the MLT and at the Bottomside F Layer and their Potential Contributions to Neutral and Plasma Dynamics"	
	5a. CONTRACT NUMBER FA9550-09-C-0197
	5b. GRANT NUMBER
	5c. PROGRAM ELEMENT NUMBER

6. AUTHOR(S) D.C. Fritts	
	5d. PROJECT NUMBER
	5e. TASK NUMBER
	5f. WORK UNIT NUMBER

7. PERFORMING ORGANIZATION NAME(S) AND ADDRESS(ES) NorthWest Research Associates PO Box 3027 Bellevue, WA 98009-3027	8. PERFORMING ORGANIZATION REPORT NUMBER NWRA-12-RB459

9. SPONSORING / MONITORING AGENCY NAME(S) AND ADDRESS(ES) Dr. Cassandra Fesen Air Force Office of Scientific Research 875 N. Randolph St. Suite 325, RM 3112 Arlington, VA 22203	10. SPONSOR/MONITOR'S ACRONYM(S) AFOSR
	11. SPONSOR/MONITOR'S REPORT

12. DISTRIBUTION / AVAILABILITY STATEMENT

DISTRIBUTION A. Approved for public distribution unlimited.

13. SUPPLEMENTARY NOTES

14. ABSTRACT

Research performed under this AFOSR contract targeted anticipated neutral atmosphere influences on the seeding, character, and statistics of equatorial plasma bubbles (EPBs). We employed several approaches, including 1) a large measurement program in Brazil, 2) analyses of correlative satellite data, and 3) numerical modeling of gravity wave dynamics that we expect to have significant influences on plasma dynamics in the ionosphere. Our SpreadFEx-2 field program focused on the onset of the EPB season, ~October to December of 2009, 2010, and 2011 and employed much enhanced instrumentation compared to our 2005 SpreadFEx measurements. Enhancements included 1) FPIs measuring F-layer winds in Brazil, 2) 6300 imagers enabling tomography of EPB structures, and 3) CERTO beacon receivers for correlative studies with the C/NOFS satellite. The FPIs and imagers demonstrated the relative motions between neutral winds and EPBs to be a function of time and likely altitude. CHAMP data revealed the nature of the migrating tides at ~400 km, their variations with season and the solar cycle, and the seasonal variations in gravity wave responses at ~300 km during 2010. Numerical studies of gravity waves addressed instability dynamics and penetration from specific sources that we expect to be especially important in the ionosphere.

15. SUBJECT TERMS

Equatorial plasma bubbles, EPB season, solar cycle, gravity waves, ionosphere, layer winds

16. SECURITY CLASSIFICATION OF: NONE			17. LIMITATION OF ABSTRACT	18. NUMBER OF PAGES	19a. NAME OF RESPONSIBLE PERSON David C. Fritts
a. REPORT	b. ABSTRACT	c. THIS PAGE		12	19b. TELEPHONE NUMBER *(include area code)* 425-556-9055

Standard Form 298 (Rev. 8-98)
Prescribed by ANSI Std. 239.18